REPORT DOCUMENTATION PAGE

Form Approved OMB No. 0704-0188

1. REPORT DATE *(DD-MM-YYYY)*	2. REPORT TYPE	3. DATES COVERED *(From – To)*
30 Sep 03	Final Report	4 September 2001 - 04-Nov-03

4. TITLE AND SUBTITLE

Predicting the effect of defect distributions in the bulk and on surfaces of ceramic materials

5a. CONTRACT NUMBER
F61775-01-WE064

5b. GRANT NUMBER

5c. PROGRAM ELEMENT NUMBER

6. AUTHOR(S)

Professor Robin W. Grimes

5d. PROJECT NUMBER

5d. TASK NUMBER

5e. WORK UNIT NUMBER

7. PERFORMING ORGANIZATION NAME(S) AND ADDRESS(ES)

Imperial College, London
Prince Consort Road
London SW7 2BP
United Kingdom

8. PERFORMING ORGANIZATION REPORT NUMBER

N/A

9. SPONSORING/MONITORING AGENCY NAME(S) AND ADDRESS(ES)

EOARD
PSC 802 BOX 14
FPO 09499-0014

10. SPONSOR/MONITOR'S ACRONYM(S)

11. SPONSOR/MONITOR'S REPORT NUMBER(S)
SPC 01-4064

12. DISTRIBUTION/AVAILABILITY STATEMENT

Approved for public release; distribution is unlimited.

20040210 125

13. SUPPLEMENTARY NOTES

14. ABSTRACT

This report results from a contract tasking Imperial College, London as follows: The contractor will investigate and ultimately develop ways to select optimum compositions for materials using atomic scale computer simulation. The particular material systems to be studied are: pyrochlores and fluorites (important in fuel cell and oxygen generator applications and as thermal barrier coatings on turbine blades in jet engines), and the perovskites, important electronic ceramics that also act as catalysts. The work proposed here falls into two categories: those associated with the behavior of defects within the bulk or interior, and those associated with surface structures. The contractor shall: Investigate solution of aliovalent dopant ions in pyrochlore oxides. Predict the extent of disorder in pyrochlore oxides. -Identify compositions that exhibit complex defect behavior in perovskite oxides. Predict surface hydroxylation of yttria stabilized ZrO2. Investigate how surface tension is changed by hydroxylation of ZrO2 surfaces.

15. SUBJECT TERMS
EOARD, Materials, Ceramics, Computational Materials, fuel cell, coating

16. SECURITY CLASSIFICATION OF:			17. LIMITATION OF ABSTRACT	18, NUMBER OF PAGES	19a. NAME OF RESPONSIBLE PERSON
a. REPORT	b. ABSTRACT	c. THIS PAGE			CHARLES H. WARD, Lt Col, USAF
UNCLAS	UNCLAS	UNCLAS	UL	24	19b. TELEPHONE NUMBER *(Include area code)* +44 (0)20 7514 3154

Predicting the effect of defect distributions in the bulk and on surfaces of ceramic materials

Mark R. Levy and Robin W. Grimes

Dept. of Materials, Imperial College, London SW7 2BP, UK.

Contract No. : F61775-01-WE064
Date - From : 1st April 2003
Until : 31st October 2003

Executive Summary

Following on from the work on the pyrochlore materials ($A_2B_2O_7$), we have extended the contour map approach by application to a wider range of perovskite related materials with the general formula ABO_3. Intrinsic defect processes were compared within this extensive range of $A^{3+}B^{3+}O_3$ compounds with A cation radii varying from Sc^{3+} to La^{3+} and B cation radii from Al^{3+} to In^{3+}. A change in preference between cation antisite, Schottky and oxygen Frenkel disorder are predicted as a function of cation radius and trends have been explained in terms of variations in lattice energy and changes in crystal structure. Of particular interest was the unexpected result that some defect processes mirror changes in crystal structure while others change smoothly across crystal boundaries.

This work fulfils a commitment in the original contract to "Identify compositions that exhibit complex defect behaviour in perovskite oxides."

Introduction

Due to their many actual and potential technological applications, perovskite materials have been investigated extensively [1-6]. Initially much of this prior work considered 2:4 perovskites, for example the original perovskite compositions $Ca^{2+}Ti^{4+}O_3$ and the ferroelectric phase $Ba^{2+}Ti^{4+}O_3$ [7, 8]. Nevertheless ABO_3 compositions in which both the A and B cations assume 3+ formal charge states are also of considerable importance with applications as microwave dielectrics [9], sensors [10, 11] and solid oxide fuel cells (SOFC's) [1]. In all cases the application is facilitated by inducing defects (in some cases via dopanting) within the perovskite lattice.

Here our interest is focused on intrinsically pure materials as a first step towards a broader understanding of defects generally. For example, when the lattice is disordered, defects on the cation sublattice will remain due to their mobiliy being much lower than those generated on the oxygen sublattice (which are known to be mobile since these materials are used as anodes in SOFC's due to their high oxygen ion conductivities). One of the more common defect processes on the cation sublattice is the antisite reaction, where the A and B cations are swapped. For materials such as $(Ca,Sr)TiO_3$, where the charges on the A and B cations are not equivalent, a considerable charge redistribution will be introduced into the lattice with intense associated strains. An additional factor contributing to the lattice strain is the significant size difference between the A and B cations.

Here we extend the studies of disorder processes in pyrochlores to the perovsites by considering ABO_3 materials in which the A and B cations both assume formal 3+ valence states. One of the primary motivations for studying these 3:3 compounds is

that cation disorder does not lead to a charge imbalance. It may be that the equivalence of the charge states leads to lower disorder energies; however, for many perovskites we are still faced with a significant cation size difference.

We will consider an exceptionally broad range of ABO_3 compositions with the A cation ranging from Sc^{3+} (1.05Å) to La^{3+} (1.34Å) and the B cation ranging from Al^{3+} (0.535Å) to In^{3+} (0.8Å). Consequently, at one extreme of the compositional range the A and B cations are of very similar size. Such $A^{3+}B^{3+}O_3$ compositions no longer exhibit a perovskite like structure, but take on the cubic bixbyite structure.

In this study, atomic scale computer simulation techniques are used to predict the structures and energies associated with defect formation in these 3:3 compounds. Those structures which exhibit larger energies for disorder processes will assume a greater residual or retained energy upon disorder and on this basis are assumed less tolerant of such defects [12]. Such an approach has proved successful in earlier work at predicting the relative structure boundary between pyrochlore (in which the cations are ordered) and fluorite (in which the cations are disordered) [12]. The approach was also successful in predicting the order / disorder transformation in $A_2H_fO_7$ compositions [13] and nonstoichiometry across the entire $A_2B_2O_7$ compositional range [14].

Methodology

The calculations presented here are based upon a classical Born-like description of an ionic crystal lattice [15]. The interatomic forces acting between ions are resolved into two terms: long-range Coulombic, which were summed via the Ewald method [16], and short-range pair terms, which were modelled using parameterised Buckingham pair potentials [17]. The perfect lattice is defined by tessellating the unit cell throughout space using periodic boundary conditions as defined by the crystallographic lattice vectors. The lattice energy (E_L) can then be expressed as follows:

$$U_L = \frac{1}{4\pi\varepsilon_0}\sum_{i\neq j}\frac{q_i q_j}{r_{ij}} + Ae^{\frac{-r_{ij}}{\rho}} - \frac{C}{r_{ij}^6} \qquad \textbf{Equation 1}$$

where A_{ij}, ρ_{ij} and C_{ij} are the adjustable parameters, r_{ij} are the interionic separation and q_i, q_j are the charges on ions i and j respectively. The parameters of the short-range potential were derived using a multi-structure-fitting procedure, described elsewhere [18, 19], and are reported in Table 1.

Table 1. Potential parameters used[19, 20].

Species	A (eV)	ρ (Å)	C (eVÅ^6)
O^{2-} - O^{2-}	9547.96	0.2192	32
Al^{3+} - O^{2-}	1365.79	0.30096	2.538
Cr^{3+} - O^{2-}	1452.28	0.30918	4.472
Ga^{3+} - O^{2-}	1456.72	0.30988	4.616
Fe^{3+} - O^{2-}	1478.98	0.31306	6.960
Sc^{3+} - O^{2-}	1587.95	0.32190	8.143
In^{3+} - O^{2-}	1595.65	0.32960	7.402
Lu^{3+} - O^{2-}	1561.36	0.33854	10.01
Yb^{3+} - O^{2-}	1616.68	0.33798	13.34
Er^{3+} - O^{2-}	1678.21	0.33781	10.34
Y^{3+} - O^{2-}	1721.23	0.33821	10.29
Gd^{3+} - O^{2-}	1868.75	0.33880	11.62
Eu^{3+} - O^{2-}	1886.71	0.33975	11.997
Sm^{3+} - O^{2-}	1944.44	0.34080	12.49
Nd^{3+} - O^{2-}	1979.11	0.34148	13.07
Pr^{3+} - O^{2-}	2025.54	0.34270	13.83
Ce^{3+} - O^{2-}	2034.18	0.34380	15.86
Tb^{3+} - O^{2-}	1818.00	0.33845	14.33
Dy^{3+} - O^{2-}	1767.64	0.33770	10.94
Ho^{3+} - O^{2-}	1726.29	0.33776	10.72
La^{3+} - O^{2-}	2051.32	0.34585	15.51
Pu^{3+} - O^{2-}	1152.00	0.37480	12.10

Table 2. Shell Parameter for O^{2-}[19, 20].

Species	Y (e)	*k* (eVÅ^{-2})
O^{2-}	-2.04	6.3

In order to investigate the radiation tolerance of the perovskite materials, lattice defects must be considered, and their relative energies assessed. However, defect energies involve a contribution due to lattice relaxation. This relaxation is greatest close to the defect. Therefore, the lattice is partitioned into spherical, concentric regions [21]. The defect is placed at the centre of Region I and the ions are relaxed explicitly using a Newton-Raphson procedure. Region IIa is an interfacial region in which the forces between ions are determined via the Mott-Littleton approximation [21, 22] and all ions are relaxed in a single step, whilst the interaction energies between the ions in region IIa and region I are calculated explicitly. Finally, the outer region IIb is effectively a point charge array that provides the Madelung field of the remaining crystal. The relaxation energy of region IIb is approximated via the Mott-Littleton approximation [23]. In these calculations, the radius of Region I is 10 Å and that of Region IIa is 31 Å. All calculations were carried out using the GULP code [24, 25].

The electronic polarisability of oxygen ions is accounted for via the shell model [26]. For the purposes of this study we have used a massless shell with charge Y = -2.04 |e|, is coupled to a core of charge X=+0.04 |e|, via an isotropic harmonic spring with force constant, k = 6.3 eVÅ^{-2}.

Results and Discussion

Crystallography

Our traditional view of the perovskite lattice is that it consists of small B cations within oxygen octahedra, and larger A cations which are XII fold coordinated by oxygen. This structural family is named after the mineral $CaTiO_3$ which exhibits an orthorhombic structure with space group Pnma [7]. For the $A^{3+}B^{3+}O_3$ perovskites the most symmetric structure observed is rhombohedral $R\bar{3}c$ (e.g. $LaAlO_3$) which involves a rotation of the BO_6 octahedra with respect to the cubic structure. However, this distortion from the perfect cubic symmetry is slight [27].

One measure of the propensity for a composition to adopt a high symmetry structure is the classical tolerance factor, t. This is defined in equation 2 where R_A, R_B, and R_O are the relative ionic radii of the A site cations, B site cations, and oxygen ions respectively [28].

$$t = \frac{R_A + R_O}{\sqrt{2}(R_B + R_O)} \qquad \textbf{Equation 2}$$

The tolerance factor will be equal to 1 if the A and B cations fit exactly into a perfect cubic packing of oxygen octahedra. It is therefore not surprising that $LaAlO_3$ adopts the highly symmetric $R\bar{3}c$ structure since its tolerance factor is 1.00, based on the appropriate VI and XII coordinate radii of Shannon [29]. As the A cation radius decreases and/or B cation radius increases, the tolerance factor decreases. In the perovskite structure, this is associated with the octahedral tilting to yield lower symmetry arrangements which, in the first instance, gives rise to an orthorhombic

structure with space group Pnma. Even greater deviations lead to a structure with hexagonal $P6_3cm$ crystallography [30]. In this final so called perovskite variant, the distortions are so great that the A cations are now essentially VII coordinate and the B cations are V coordinate. As such it is not clear that this so called perovskite is very perovskite like!

Beyond this hexagonal regime, all resemblance to the perovskite structure is lost and a cubic bixbyite is formed with Ia3 symmetry. Here the A and B cation radii are very similar, both cation sites are VI coordinated by oxygen. Although dissimilar to perovskite, it is possible to consider bixbyite in terms of a defective fluorite structure [31].

In order to elucidate trends, we must compare all compositions in a single figure. This can be achieved if the A cations are ordered by size (assuming the XII coordinate radii values throughout) along an x-axis and the B cations (using the VI coordinate values) along a y-axis, thereby forming a 2D grid of compounds. Such a plot is shown in figure 1 for all 96 compounds for which calculations were performed. Of course, for the $P6_3cm$ and Ia3 structures, the cations are not XII and VI coordinated, however to allow for comparison the XII and VI coordinate radii are used throughout. In this case therefore, the radii simply represent an order parameter.

The lattice energy for each compound was calculated according to equation 1, assuming each of 17 possible crystal structures reported in the literature for materials with the BO_3 stoichiometry (including the four mentioned above). From these data the lowest lattice energy is identified for each compound so that an energy value is

assigned to each composition. Each composition is also identified in figure 1 by a symbol which indicates its lowest energy structure (e.g. a square for bixbyite etc.). Lattice energy contours were then generated using software [32], which connects equal energy values over the cation radii surface. Such maps facilitate comparisons and allow identification of compositional ranges that are of particular significance. In this case it is at once clear that the compounds fall into four groups: rhombohedral $R\bar{3}c$, orthorhombic Pnma, hexagonal $P6_3cm$, and bixbyite Ia3. In this regard it is important to note that although 17 different crystal structures have been reported for ABO_3 compounds in general, some have only been reported for $A^{2+}B^{4+}O_3$ materials and others represent only slight distortions from those already mentioned.

Our predictions of structural types are in overall agreement with experimental data and are consistent with changes in the tolerance factor (see figure 2). In particular, where we predict an orthorhombic structure, experimental structures are known to be orthorhombic in most cases. The same holds true for the hexagonal and rhombohedral structures. However, within the orthorhombic and hexagonal regimes, certain compounds are reported experimentally to exhibit slight variations from Pnma and $P6_3cm$ respectively. Furthermore, a few compositions in the centre of the map, such as $YFeO_3$, do not form an ABO_3 material, but disproportionate into garnet structures.

Disorder Processes

Once the lowest energy lattice structure has been identified, the individual component defect energies were calculated. Then each compound can be assigned Schottky, oxygen Frenkel or antisite defect process energies by following the total defect processes described in equations 3, 4 and 5 below.

$$"null" \rightarrow V_A''' + V_B''' + 3V_O^{\bullet\bullet} \qquad \textbf{Equation 3}$$

$$O_O^X \rightarrow O_i'' + V_O^{\bullet\bullet} \qquad \textbf{Equation 4}$$

$$A_A^X \rightarrow A_i^{\bullet\bullet\bullet} + V_A''' \qquad \textbf{Equation 5}$$

The calculated values for A and B cation Frenkel energies are far higher than those for Schottky, oxygen Frenkel and antisite reactions, and as such will not be considered further. In a similar manner as described for perfect lattice energies, defect process energies can be represented over the full compositional range on an energy contour map (see figures 3, 4 and 5 which use the same energy contour interval). Low energy regions identify compounds for which the defect process is more favourable. In order to allow for comparison between the different defect reactions, the energies presented are normalised per defect, as dictated by a mass action analysis [33], i.e. the Schottky process has a normalisation factor of 5, whilst the antisite and oxygen Frenkel processes have normalisation factors of 2.

Returning to the Schottky, oxygen Frenkel and antisite reactions, comparing figures 3, 4 and 5, it is at once apparent that the Schottky and oxygen Frenkel disorder processes show less variation in energy as a function of cation radii than the antisite process. Although the tolerance factor was originally derived to predict the distortion of a perovskite lattice from an idealised cubic structure, we can also use it to understand the variation exhibited by the antisite energy. This is because the tolerance factor is actually a relative measure of the difference in size of the A and B cations and by inference how much distortion would be necessary to accommodate an A cation at a B

site and vice-versa (i.e. as in the antisite reaction). In this regard, we find it convenient to quantify this for the perovskite compositions alone, such that low t values (i.e. less than 0.8) indicate that the cations fit fairly well in each others sites, while high t values (i.e. greater than 0.8) suggest that they fit rather less well. Thus the value for a perfect cubic perovskite (i.e. 1) would imply a high antisite energy. By comparing figures 2 and 5, it is clear that there is an excellent correlation between our calculated antisite energy and the tolerance factor.

The smaller predicted variation in Schottky energy as a function of cation radius is a consequence of competing factors. In the Schottky reaction (equation 3) the displaced ions form new lattice and as such, the lattice energy and hence its variation with component cation radii is an important factor. This was shown in figure 1 and clearly the lattice energy gain is greatest for compositions in the bottom left hand corner. The second term concerns the energy to form vacancies. Higher energies (less favourable) will result in materials with higher Madelung or electrostatic energies. Although these vary somewhat between structure types, values principally increase as the interatomic separation decreases. As such we expect higher energies in the bottom left hand corner, i.e. the opposite variation observed with the lattice energy (see figure 1). These electrostatic terms are therefore working in opposition, and the net effect is a smaller variation in Schottky energy as a function of cation radii. Contributions from the short range pair energies now become important. Consequently structure type boundaries where there is a change in ion coordination should show up in the Schottky energy map. In figure 3, we show evidence of such a change between Pnma (VI, XII) and $P6_3cm$ (V, VII) but not $R\bar{3}c$ (VI, XII) to Pnma (VI, XII).

By comparing the results in figures 3 and 5 it is at once evident that there is a change in lowest disorder process energy from Schottky to antisite as a function of the cation radii. If we express this in terms of the tolerance factor, the swap-over occurs at a t value between 0.99 and 0.98 with the antisite reaction dominant for all lower values. Thus, only in a small portion of the cation radii space (i.e. at the bottom right) does Schottky disorder dominate over antisite. Furthermore, in this region, the difference in process energies is not great, and thus materials such as $LaAlO_3$ should exhibit complex defect equilibria. We can also compare the oxygen Frenkel and antisite energies. The oxygen Frenkel energy decreases somewhat as the A cation radius increases and the B cation radius decreases, in a similar manner to the antisite process energies. The oxygen Frenkel energy decreases somewhat as the A cation radius decreases and the B cation radius increases, in a manner similar to the antisite process. Although it does drop to a value considerably below the Schottky for a majority of the compositional range, the oxygen Frenkel energy does not decrease to the same extent as the antisite and is never the dominant defect process. Again we see some evidence of the Pnma to $P6_3cm$ structure change.

Comparison to Pyrochlore/Fluorite

The perovskite defect process energies can now be compared to the equivalent lowest energy defect process energies in other materials. Here we can make that comparison to the fluorite and pyrochlore oxides investigated previously [12, 19]. In this case, the antisite energies of the perovskites are well above those for the zirconium containing pyrochlore/fluorite materials (e.g. $Er_2Zr_2O_7$ (0.6 eV) and $Gd_2Zr_2O_7$ (1.8 eV) [12]). As such, only selected $P6_3cm$ perovskites will exhibit defect concentrations as high as the zirconate pyrochlores. On the other hand, the titanate pyrochlores exhibit antisite

defect energies of typically 2.9 eV which is equivalent to the lowest energy for the Pnma perovskites.

The oxygen Frenkel defect energies for the perovskites (figure 4) are again higher than those for the pyrochlores. For example, the zirconate pyrochlores $Er_2Zr_2O_7$, $Gd_2Zr_2O_7$ exhibit oxygen Frenkel energies of 2.5 eV and 2.0 eV respectively [19], both being lower than any of the perovskite materials. However, the titanate pyrochlores have values that are similar to the Pnma perovskites, for example, $Gd_2Ti_2O_7$ has an oxygen Frenkel energy of 5.6 eV [19]. Consequently, values for the bixbyites, which are as low as 3 eV, compare favorably to the titanate pyrochlores and are not significantly higher than the zirconates.

Up to this point we have suggested a model that considered only isolated defects. However, the stability of such defects depend not only on their individual energies, but also on the interactions between them. This is characterised by the reduction in formation energy when the defects are associated (known as the binding energy). The work on pyrochlores considered the representative defect cluster $\{A_B^X : B_A^X : V_O^{\bullet\bullet} : O_i''\}^X$, a combination of antisite and oxygen Frenkel reactions where the defects are in their nearest neighbour positions [19]. Interestingly, when different geometries of this cluster are investigated for pyrochlore, the oxygen Frenkel component somtimes self annihilates around the cation antisite pair. Such behaviour was not observed in equivalent perovskite clusters. This may in itself be a significant difference between pyrochlores and perovskites in regard to their ability to accommodate large defect populations. Nevertheless, in order to compare equivalent defect clusters, here we simply compare energies for adjacent antisite pairs

$\{A_B^X : B_A^X\}^X$ (see table 3 for examples). Critically, for perovskites the value when the defects are associated (i.e. clustered) are only modestly less than when the defects are isolated).

Table 3. Comparison of the total defect energies for isolated defects and clusters for different compositions of perovskite and pyrochlore oxides. N.B. the energies in this table have not been normalised to facilitate comparisons.

	Total Defect Energy (eV) $\{A_B^X : B_A^X\}^X$	
	Isolated	**Clustered**
Perovskite		
$GdAlO_3$	8.20	7.05
$LaAlO_3$	11.98	10.59
$GdFeO_3$	4.24	4.03
$LaFeO_3$	7.44	6.30
Pyrochlore [2]		
$Gd_2Ti_2O_7$	6.09	4.98
$La_2Ti_2O_7$	5.94	4.59
$Gd_2Zr_2O_7$	3.68	2.86
$La_2Zr_2O_7$	4.52	3.45

Conversely, in pyrochlore materials, cluster formation values are considerably less than for isolated defects (again see table 3). The larger binding energy for pyrochlores now means that we see a significant difference between the antisite energy for $GdFeO_3$ compared to lower zirconate pyrochlore values. The other perovskites maintain their higher defect process energies.

Clearly, for the pyrochlore materials, these antisite defects are more strongly bound than for the perovskite materials. This may well imply that in perovskites, as the defect concentrations increase, the retained energy increases more quickly. On this basis, all the perovskites should accommodate lower defect concentrations than pyrochlores. However, to be definitive would require better analysis probably using a molecular dynamics approach (because of the great number of cluster configurations).

Conclusion

As a consequence of the broad compositional range of ABO_3 materials considered, the assumed crystal structures of individual compositions varies considerably from rhombohedral $R\bar{3}c$ when the A and B cation radii are most different, to orthorhombic Pnma, to hexagonal $P6_3cm$, and finally to the cubic bixbyite Ia3 as the constituent cation radii converge. Despite this drastic change in the crystallography of the system, a smooth transition in the lattice energy across these structural boundaries is predicted (see figure 1).

As a first approximation to understanding the variation in crystal structure, the classical tolerance factor provides an important benchmark. The tolerance factor follows the changes remarkably well and infers that the atomistic simulation results are in agreement with classical perovskite theory (see figure 2).

The structural changes also manifest themselves in the defect chemistry of these ABO_3 materials. The defect process energies of the Schottky and oxygen Frenkel reactions show abrupt changes in compositional regions (i.e. cation radii space) associated with changes in crystal structure (see figures 3 and 4). Conversely in the antisite reaction energy decreases smoothly and rapidly as a function of the component cation radii across crystal structure boundaries (see figure 5).

For compounds with large A cation radii and small B cation radii (i.e. the lower right hand corner of the maps) the Schottky defect reaction is the dominant (lowest energy) process, whereas for the rest of the compositional range the antisite process dominates. However, if one considers defect processes on just the oxygen sublattice,

there is also a change over in the dominant reaction from Schottky to oxygen Frenkel that occurs close to the orthorhombic Pnma to hexagonal $P6_3cm$ crystal structure boundary. Such process mechanisms are important because such defect reactions on the oxygen sublattice control the equlibria which provide the defects that mediate transport mechanisms of oxygen through the lattice.

In an attempt to understand the interplay between defects on the cation and anion sublattices, defect clusters have been considered that combine a cation antisite defect pair with an oxygen Frenkel pair. The clusters in perovskite have been compared to equivalent clusters investigated previously in the pyrochlore materials. One of the startling differences between the two structures is that within the pyrochlore materials, different geometries of the cluster lead to the annihilation of the oxygen Frenkel pair vastly reducing the energy of the cluster. Such mechanisms were not seen in the perovskite materials. Partly as a consequence, a different cluster formed from an adjacent antisite defect pair was considered to allow for comparison between the perovskite and pyrochlore. Here, the energies for clustered defects in the perovskites are only modestly lower than when the defects are isolated, conversely, the equivalent cluster within the pyrochlore materials is much lower in energy than the isolated defects. As such the antisite defects are more strongly bound together in the pyrochlore material than the perovskite. This implies that as the defect concentrations increase within perovskites, the retained energy increases rapidly and as such the perovskites should not be able to accommodate such large defect concentrations as the pyrochlore material

References

1. Skinner, S.J., *Recent advances in Perovskite-type materials for solid oxide fuel cell cathodes.* International Journal of Inorganic Materials, 2001. **3**(2): p. 113-121.
2. Mathur, N. and R.M. Thomas, *Power to perovskite.* New Scientist, 1998. **158** (2132): p. 30-33.
3. Norby, T., *Solid-state protonic conductors: principles, properties, progress and prospects.* Solid State Ionics, 1999. **125**(1-4): p. 1-11.
4. Martinez-Ortega, F., et al., *Methane catalytic combustion on La-based perovskite catalysts.* Comptes Rendus De L Academie Des Sciences Serie Ii Fascicule C- Chimie, 2001. **4**(1): p. 49-55.
5. Islam, M.S. and M. Cherry, *Protons in $LaMO_3$: Atomistic modelling and ab initio studies.* Solid State Ionics, 1997. **97**(1-4): p. 33-37.
6. Knauth, P. and H.L. Tuller, *Solid-state ionics: Roots, status, and future prospects.* Journal of the American Ceramic Society, 2002. **85**(7): p. 1654-1680.
7. Glazer, A.M., *The Classification of Tilted Octahedra in Perovskites.* Acta Cryst., 1972. **B28**: p. 3384-3392.
8. Muller, O. and R. Roy, *The Major Ternary Structural Families.* Crystal Chemistry of Non-Metallic Materials: Springer-Verlag.
9. Ivanova, V.V., et al., *Synthesis and properties of $BiFeO_3$-$DyMnO_3$ solid solutions.* Inorganic Materials, 2003. **39**(7): p. 745-748.
10. Kersen, U., *Microstructural and surface characterization of solid state sensor based on $LaFeO_3$-sigma oxide for detection of NO_2.* Analyst, 2001. **126**(8): p. 1377-1381.

11. Ge, X.T., Y.F. Liu, and X.Q. Liu, *Preparation and gas-sensitive properties of $LaFe_{1-y}Co_yO_3$ semiconducting materials.* Sensors and Actuators B-Chemical, 2001. **79**(2-3): p. 171-174.

12. Sickafus, K.E., et al., *Radiation tolerance of complex oxides.* Science, 2000. **289**(5480): p. 748-751.

13. Stanek, C.R. and R.W. Grimes, *Prediction of rare-earth $A_2Hf_2O_7$ pyrochlore phases.* Journal of the American Ceramic Society, 2002. **85**(8): p. 2139-2141.

14. Stanek, C.R., L. Minervini, and R.W. Grimes, *Nonstoichiometry in $A_2B_2O_7$ pyrochlores.* Journal of the American Ceramic Society, 2002. **85**(11): p. 2792-2798.

15. Born, M., *Atomtheorie des Feten Zustandes*. 1923, Teubner, Leipzig, Germany.

16. Ewald, P.P., Ann. Physik, 1921. **64**: p. 253.

17. Buckingham, R.A., *The classical equation of state of gaseous helium, neon and argon.* Proceedings of the Royal Society of London Series A, 1938. **168**: p. 264-283.

18. Minervini, L., et al., *The oxygen positional parameter in pyrochlores and its dependence on disorder.* Philosophical Magazine a-Physics of Condensed Matter Structure Defects and Mechanical Properties, 2002. **82**(1): p. 123-135.

19. Minervini, L., R.W. Grimes, and K.E. Sickafus, *Disorder in pyrochlore oxides.* Journal of the American Ceramic Society, 2000. **83**(8): p. 1873-1878.

20. Binks, D.J., *Computer Modelling of Zinc Oxide and Related Oxide Ceramics*, in *Department of Chemistry*. 1994, University of Surrey. p. 243.

21. Mott, N.F. and R.W. Gurney, *Conduction in Polar Crystals. III. On the Colour Centres in Alkali-Halide Crystals.* Trans. Faraday Soc, 1938: p. 506-511.

22. Mott, N.F., *Conduction in Polar Crystals. II. The Conduction Band and Ultra-Violet Absorption of Alkali-Halide Crystals.* Trans. Faraday Soc., 1938: p. 500-511.

23. Mott, N.F. and M.J. Littleton, *Conduction in Polar Crystals. I. Electrolytic Conduction in Solid Salts.* Trans. Faraday Soc., 1938. **34**: p. 485-499.

24. Gale, J.D., *GULP: Technical Report.* 1994, Royal Institution of Great Britain.

25. Gale, J.D., *GULP: A computer program for the symmetry-adapted simulation of solids.* J. Chem. Soc., Faraday Trans., 1997. **93**(4): p. 629-637.

26. Dick, B.G. and A.W. Overhauser, *Theory of the Dielectric Constants of Alkali Halide Crystals.* Phys. Rev., 1958. **112**(1): p. 90-103.

27. Muller, O. and R. Roy, *The major ternary structureal families, Crystal chemistry of non-metallic materials.* 1974: Springer-Verlag.

28. Geller, S., *Crystallographic Studies of Perovskite-Like Compounds. V. Relative Ionic Sizes.* Acta Crystallogr., 1957. **10**: p. 248-251.

29. Shannon, R.D., *Revised Effective Ionic Radii and Systematic Studies of Interatomic Distances in Halides and Chalcogenides.* Acta Crystallographica, 1976. **A32**: p. 751-767.

30. Howard, C.J. and B.J. Kennedy, *The orthorhombic and rhombohedral phases of LaGaO3 - a neutron powder diffraction study.* Journal of Physics-Condensed Matter, 1999. **11**(16): p. 3229-3236.

31. Sickafus, K.E., et al., Nuclear Instruments & Methods in Physics Research Section B- Beam Interactions with Materials and Atoms, 2002. **191**: p. 549.

32. Kerr, R.A., *Nuclear Waste Disposal: Alternatives to Solidification in Glass Proposed.* Science, 1979. **204**(4390): p. 289-291.

33. Kroger, F.A., *The Chemistry of Imperfect Crystals*. 1974, North-Holland Publishing Company, Ltd. p. 82.

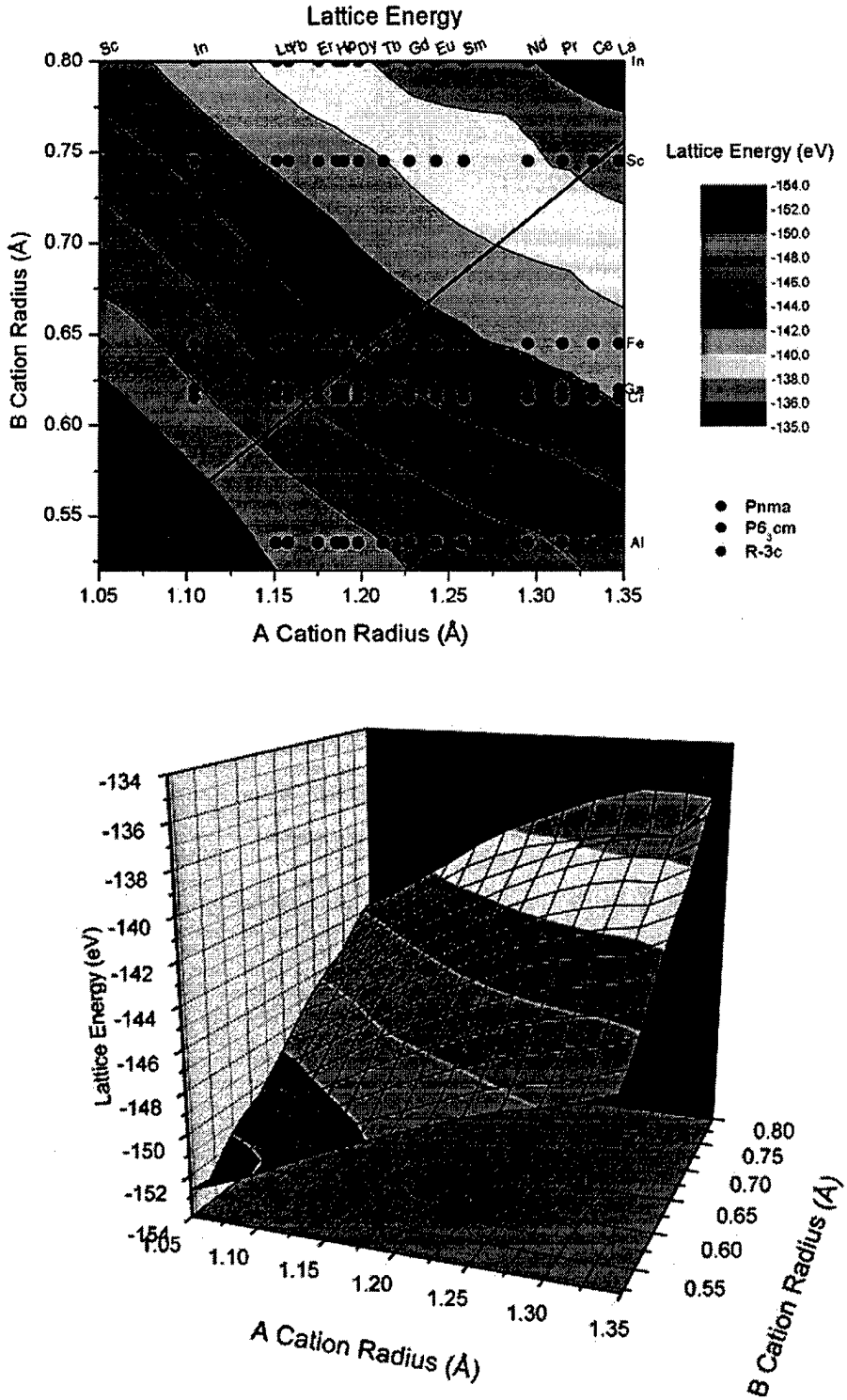

Figure 1. Lattice energy (eV) contour map.

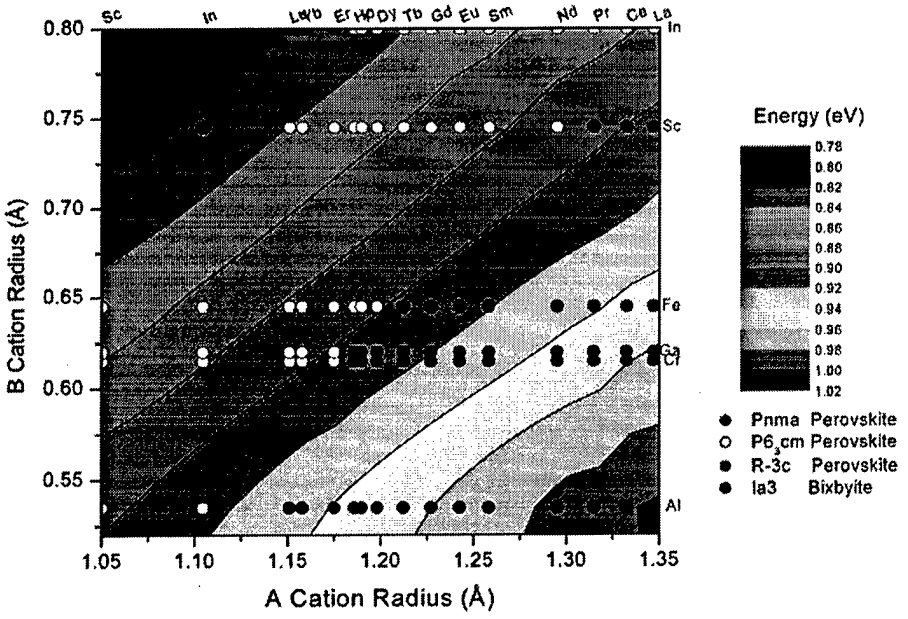

Figure 2. Classical Tolerance Factor variations asa function of cation radii.

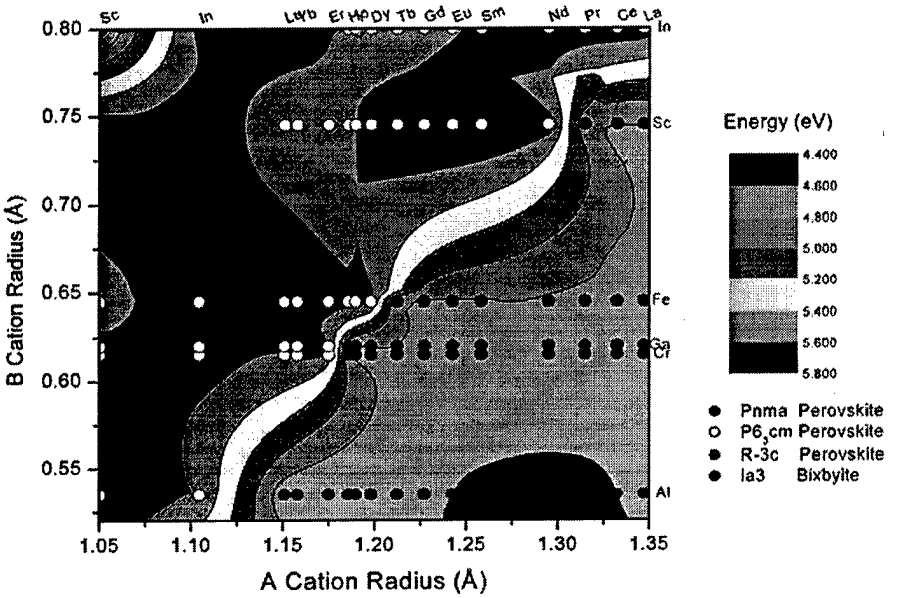

Figure 3. Schottky reaction energy Contour map.

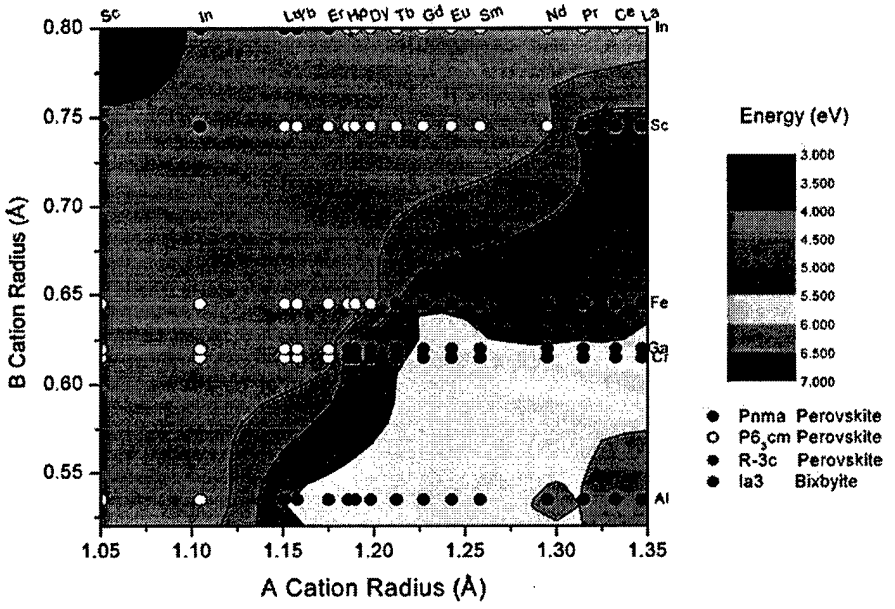

Figure 4. Oxygen Frenkel reaction energy contour map.

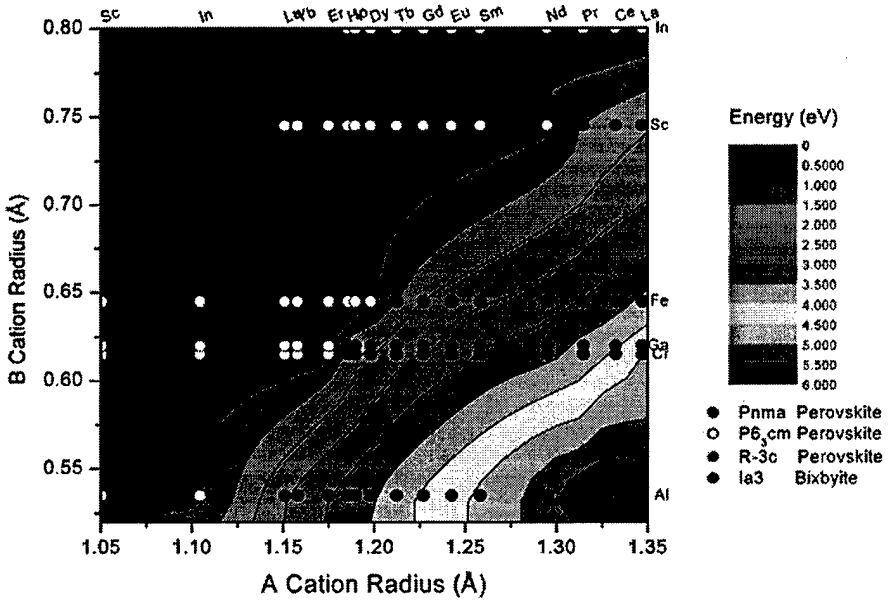

Figure 5. Antisite reaction energy contour map.

(1) In accordance with Defense Federal Acquisition Regulation 252.227-7036, Declaration of Technical Data Conformity (Jan 1997),

"The Contractor, Imperial College, hereby delcares that, to the best of its knowledge and belief, the technical data delivered herewith under Contract No. F61775-01-WE064 is complete, accurate, and complies with all requirements of the contract.

DATE: 29th Sept 2003

Name and Title of Authorized Official: Rob W. Lines

(2) In accordance with the requirements in Federal Aquisition Regulation 52.227-13, Patent Rights—Acquisition by the *U.S.* Government (Jun 1989),

(A) "~~Disclosures of all subject inventions as defined in FAR 52.227-13 have been reported in accordance with this clause.~~"

Or,

(B) "I certify that there were no subject inventions to declare as defined in FAR 52.227-13, during the performance of this contract."

DATE: 29th Sept 2003

Name and Title of Authorized Official: Prof. ROBIN W. GRIMES

Rob W. Lines